Radio Science, Volume 30, Number 5, Pages 1577–1595, September–October 1995

The feasibility of radio sounding in the magnetosphere

W. Calvert,[1] R. F. Benson,[2] D. L. Carpenter,[3] S. F. Fung,[2] D. L. Gallagher,[4] J. L. Green,[2] D. M. Haines,[5] P. H. Reiff,[6] B. W. Reinisch,[5] M. F. Smith,[2] and W. W. L. Taylor[7]

Abstract. A radio sounder outside the plasmasphere could provide nearly continuous remote density measurements of the magnetopause and plasmasphere, as well as other important density features elsewhere in this region. Using digital integration and tuned reception at frequencies from a few kilohertz to a few megahertz with 400-m to 500-m tip-to-tip dipole antennas and 10 W transmitter power, such a sounder would be capable of 10% density resolution and 500 to 1300 km spatial resolution in only a few minutes at distances of up to 4 R_E. By providing such detailed observations of its principal density structures, such a sounder would then clearly revolutionize magnetospheric research.

1. Introduction

Radio sounding uses a radio transmitter and receiver to measure the delay and direction of pulsed radio echoes from a plasma at its ordinary and extraordinary cutoff frequencies. The echo delay as a function of frequency can then be used to determine the electron density as a function of distance, and hence to measure remotely the density of a distant plasma. A satellite radio sounder would thus be ideal for measuring density structures in the magnetosphere as shown in Figure 1.

Radio sounding was pioneered for the ionosphere during the 1920s and 1930s by *Breit and Tuve* [1928] and *Appleton* [1932]. It has since become the main tool of ionospheric research using modern digital ionosondes [*Reinisch*, 1986; *Davies*, 1990; Reinisch et al., 1992] and also using satellite radio sounders during the highly successful Alouette and ISIS Topside Sounder Programs of 1960s and 1970s [*Knecht et al.*, 1961; *Schmerling and Langille*, 1969; *Franklin and Maclean*, 1969; *Jackson et al.*, 1980; *Jackson*, 1986, 1988]. Radio sounding has thus had a long and successful history, and it is now time to implement this extremely powerful technique for the magnetosphere [*Reiff et al.*, 1994; *Green and Fung*, 1994].

The utility of radio sounding is clearly demonstrated by the Alouette and ISIS Programs, which produced nearly a thousand papers and revealed in accurate detail the density structure of the ionosphere [*Jackson*, 1986]. Unlike other techniques which only measure locally, such topside sounding during a single orbit yields the complete two-dimensional profile of density down to the peak of the F layer to a precision of roughly 10% [*Nelms and Lockwood*, 1967; *Chan and Colin*, 1969; *Jackson*, 1969b]. Such measurements led to the discovery of the auroral plasma cavity at high altitudes in the auroral zone [*Benson et al.*, 1981; *Calvert*, 1981a], as well as to the first direct observations of the equatorial anomaly at low altitudes and latitudes in the ionosphere [*Lockwood and Nelms*, 1964]. It has also been used to measure densities as low as 8 cm^{-3} [*Hagg*, 1967], to detect ducted echoes from the conjugate hemisphere [*Muldrew*, 1963], and to study a wide variety of other plasma and propagation effects, including solar radio bursts [*Hartz*, 1969] and the plasma resonances excited by sounder transmitters [*Calvert and Goe*, 1963]. As suggested by Figure 1, just a few such measurements of the main density features of the magnetosphere would clearly revolutionize magnetospheric research.

Franklin and Maclean [1969] and *Calvert* et al. [1972] have previously discussed radio sounding for the plasmasphere, and *Calvert* [1981b] has suggested using ducted echoes to measure density along the magnetic field outside the plasmasphere. Thanks to modern digital techniques, tuned reception, and focusing by the magnetopause, however, it now appears feasible to measure virtually the entire magnetosphere by this technique.

[1]University of Iowa, Iowa City
[2]Goddard Space Flight Center, Greenbelt, Maryland.
[3]Stanford University, Stanford, California.
[4]Marshall Space Flight Center, Huntsville, Alabama.
[5]University of Massachusetts, Lowell
[6]Rice University, Houston, Texas.
[7]Nichols Research Corporation, Arlington, Virginia.

Paper number 95RS01731.
0048-6604/95/95RS-01731$08.00

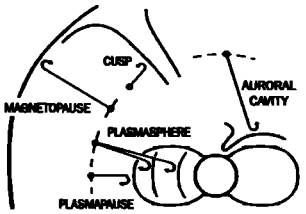

Figure 1. Main sounding targets in the magnetosphere.

A magnetospheric sounder would appear as shown in Figure 2, using three orthogonal dipole antennas to launch pulses and to measure the delay and direction of the radio echoes which return to the sounder. Long antennas are necessary for sounding and it is assumed that this satellite is spinning and equipped with two 400 m to 500 m tip-to-tip dipole wire antennas in the spin plane and a third 10 m to 20 m tubular dipole antenna along the spin axis. The two long antennas would be used for transmission and reception and the shorter antenna for reception only.

The feasibility of radio sounding in the magnetosphere will be demonstrated by estimating the echo signal strengths for such a sounder and determining the resulting density, spatial, and temporal resolution. The nature of the radio echoes used for radio sounding will be discussed in the following section, followed by a discussion of pulse transmission and echo reception in sections 3 and 4, digital integration in section 5, direction measurement and angular resolution in section 6, precision and temporal resolution in section 7, and the major factors affecting a sounder design in section 8. The conclusions will then be summarized briefly in section 9. Two appendices are also included to discuss other aspects in greater detail.

2. Radio Echoes Produced by a Sounder

2.1. Reflection

The echoes which are produced by a sounder originate at the wave cutoffs of a plasma where the refractive index goes to zero and total reflection occurs [see *Ratcliffe*, 1959; *Budden*, 1985; *Stix*, 1962; *Allis et al.*, 1963]. The reflection process is therefore coherent and the echoes which return to a sounder originate perpendicular to the refractive index contours at the point of reflection. The echo direction is thus determined by the density distribution of the target plasma and it is usually perpendicular to the magnetic field at interfaces like the plasmapause and magnetopause where the magnetic field controls the density.

2.2. Echo Frequencies

A radio sounder using dipole antennas launches a linearly polarized wave which splits into two elliptically

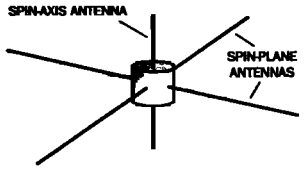

Figure 2. A magnetospheric sounder equipped with three orthogonal dipole antennas to measure echo directions.

polarized waves known as the ordinary and extraordinary waves. These two waves propagate independently and produce separate echoes which can then be distinguished by their different delay, doppler shift, and polarization. The plasma density at the point of reflection can then be determined from the frequency of either echo if the magnetic field is known, and if both echoes come from the same location, they can also be used to measure the magnetic field strength at this location.

The cutoff for the ordinary mode is at the plasma frequency:

$$f_p = \frac{1}{2\pi}\sqrt{\frac{N_e e^2}{\epsilon_0 m}} = 8.98\sqrt{N_e}\ \text{kHz} \qquad (1)$$

where N_e is the electron density per cubic centimeter, e and m are the electronic charge and mass, and ε_0 is the permittivity of free space. The cutoff for the extraordinary mode then occurs at

$$f_x = \sqrt{f_p^2 + f_g^2/4} + f_g/2 \qquad (2)$$

where

$$f_g = eB/2\pi m = 28B\ \text{kHz} \qquad (3)$$

is the cyclotron frequency and B is the magnetic field strength in microtesla.

The plasma density in the magnetosphere ranges from less than 0.1 cm^{-3} in the auroral plasma cavity and tail lobes to 10^4 cm^{-3} or more in the topside ionosphere, and the magnetic field varies from 30 to 50 microtesla (μT) in the ionosphere to roughly 30 nanotesla (nT) at the magnetopause. The plasma frequency thus varies from a few kHz to over 1 MHz, and except in the auroral plasma cavity, it is usually greater than the cyclotron frequency. The cyclotron frequency, on the other hand, varies from about 1.5 MHz in the polar ionosphere to less than 1 kHz at the magnetopause. The minimum plasma frequency in the plasma trough outside the plasmasphere, which has been measured locally with a resonance sounder by *Etcheto and Bloch* [1978], is typically about 15 kHz at geocentric distances beyond about 8 R_E, and the peak plasma frequencies at the plasmapause and magnetopause are typically 50 to 150 kHz. The plasma frequency in the plasmasphere, according to *Carpenter and Anderson* [1992], increases up to about 400 kHz at 1 R_E altitude, and plasmasphere outliers, as discussed by *Carpenter*

[1995], sometimes also occur outside the plasmasphere, as far out as 8-10 R_E with plasma frequencies often as great as 100 kHz. The relevant frequencies for radio sounding in the magnetosphere thus range from a few kilohertz to a few megahertz, with the most important echoes generally occurring in the range of 30 to 300 kHz.

2.3. Echo Delay

Although the phase velocities of the ordinary and extraordinary modes are always greater than the speed of light, the group velocity v_g, which is the speed of pulse propagation in a plasma, is approximately

$$v_g = c\sqrt{1 - f_p^2/f^2} \tag{4}$$

where the effect of the magnetic field has been neglected, **c** is the speed of light, **f** is the wave frequency, and f_p is the local plasma frequency. Outside the plasmasphere where the plasma frequency is typically 30 kHz or less according to *Etcheto and Bloch* [1978], this group velocity at 100 kHz is thus about 95% of the speed of light and the round-trip echo delay is approximately 2/**c** times the distance, or about 43 ms per Earth radii (R_E). Echo delays in the magnetosphere at distances of up to a few earth radii thus range from a few tenths of a second to a half second or more.

2.4. Echo Power Flux

In order to determine the echo signal strength for a sounder, it is necessary to calculate the echo power flux Φ_e (in watts per square meter) for a given effective radiated power **P** in the direction of the target, where the effective radiated power is the power of an equivalent isotropic source that delivers the same power flux in this direction.

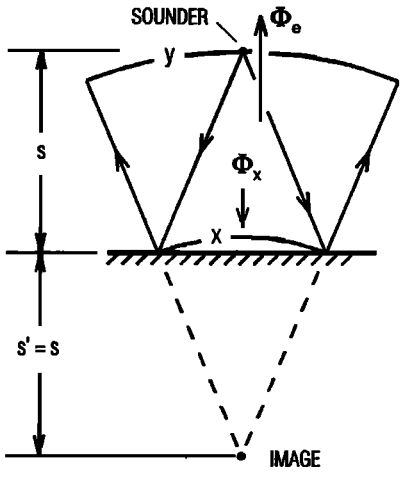

Figure 3. Coherent echo from a flat surface, where **s** is the echo distance, Φ_e is the echo power flux, and Φ_x is the transmitted power flux at the point of reflection.

2.5. Flat Targets

For a flat target, as shown in Figure 3, the power flux Φ_x at the point of reflection is

$$\Phi_x = \frac{P}{4\pi s^2} \tag{5}$$

where **P** is the effective radiated power and **s** is the target distance. Since the reflection is coherent, this flux then spreads out over a larger arc **y** = 2**x** by the time it returns to the sounder. Considering both dimensions of the wave front, the echo power flux then becomes

$$\Phi_e = \left(\frac{x}{y}\right)^2 \Phi_x = \frac{P}{16\pi s^2} \tag{6}$$

Equation (6) is the radar equation for a flat, smooth surface and applies to targets which are smooth on the scale of a wavelength and significantly larger than the diameter of the first Fresnel zone, given by $(2\lambda s)^{1/2}$, where **s** is the target distance and λ is the wavelength.

2.6. Curved Targets

In the magnetosphere, however, the radii of curvature of reflecting surfaces are often comparable to the echo distance and it is therefore necessary to determine the echo power flux for a curved target, as follows. The echo geometry then becomes that shown in Figure 4, where **s** and **s'** are the object and image distances related by the spherical mirror equation of geometric optics:

$$\frac{1}{s'} - \frac{1}{s} = \frac{2}{R} \tag{7}$$

where **R** is the surface radius of curvature, positive for a convex surface like the equatorial plasmapause and negative for concave surfaces like the magnetopause. Since

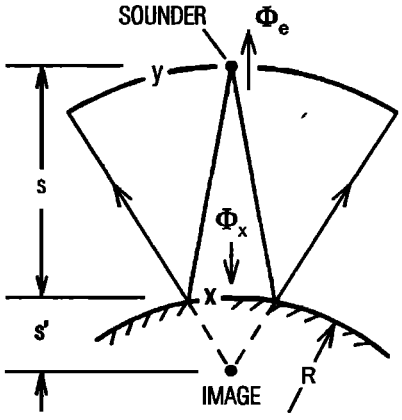

Figure 4. Echo geometry for curved targets, where **R** is the radius of curvature and **s'** is the image distance.

the arcs **x** and **y** in Figure 4 subtend the same angle at the image of the source:

$$\frac{y}{x} = \frac{s + s'}{s'} = 2\left[1 + \frac{s}{R}\right] \quad (8)$$

and the echo power flux then becomes

$$\Phi_e = \frac{P}{16\pi s^2 |1 + s/R_1||1 + s/R_2|} \quad (9)$$

where $\mathbf{R_1}$ and $\mathbf{R_2}$ are the principal radii of curvature and the absolute-value bars have been introduced to keep this flux positive when the sounder is outside the center of curvature of a concave surface like the magnetopause, where **R** is negative and **-R** is less than **s**.

Equation (9) is the radar equation for a target of arbitrary curvature. For **R** » **s** it becomes Equation (6), whereas for **R** « **s** it becomes the classical radar equation for a small target, which is usually expressed in the form $\Phi_e = \sigma P/16\pi^2 s^4$, where $\sigma = \pi R_1 R_2$ is the target cross section, equal to the area of an ellipse having $\mathbf{R_1}$ and $\mathbf{R_2}$ as its semimajor and semiminor axes.

These equations require negligible absorption and a smooth reflecting surface. The absorption, however, is expected to be negligible in the magnetosphere because of its low electron-ion and electron-neutral collision frequencies. According to *Franklin and Maclean* [1969, sect. L, p. 904], refraction can also be allowed for by substituting the virtual range for the actual echo distance, where the virtual range is the apparent echo distance at the speed of light. *Franklin and Maclean* [1969] have also verified Equation (6) using Alouette II, finding the actual echoes up to ten times stronger than predicted and attributing this difference to scattering by density irregularities as discussed by *Petrie et al.* [1965]. The effect of density irregularities is also discussed in Appendix A. *Davies* [1990, sect. 7.3.4] has also discussed focusing in the ionosphere using the one-dimensional equivalent of Equation (9), and Equation (9) has also been verified by three-dimensional ray tracing.

2.7. Relative Echo Flux

It is convenient to define the relative echo flux Φ_e/P according to Equation (9). This quantity, which represents the echo geometry independently of transmitter power, has the units of inverse meters squared and depends only on $\mathbf{R_1}$, $\mathbf{R_2}$, and **s**. The echo field strength in watts per square meter can then be calculated by multiplying by **P**, where **P** is the effective radiated power determined in section 3.

2.8. Magnetopause

As shown in Figure 1, the magnetopause will be approximated by a 10-R_E Earth-centered sphere. For a sounder at 6 R_E geocentric altitude, the echo distance is then $s = 4 R_E$, and magnetopause radii of curvature are $R_1 = R_2 = -10 R_E$. The relative flux for the magnetopause is then 8.5×10^{-17} m^{-2}, and since the magnetopause is an abrupt density step, this flux should be independent of frequency. In addition, since the sounding distance and radii of curvature are also assumed to be constant in this approximation, it will also be independent of position as the satellite moves to different latitudes and longitudes between the Earth and magnetopause on the front side of the magnetosphere.

The 1/(1+s/R) factors in Equation (9) represent focusing at the magnetopause, causing echoes which are about 2.8 times stronger than those for a flat surface. Comparable defocusing also occurs at the equator for the plasmapause, as discussed below in section 2.9. As a result, the echoes from the magnetopause turn out to be stronger than the corresponding echoes from the plasmapause, despite its greater distance.

Such focusing also increases with the magnetopause standoff distance, since **s/R** in Equation (9) is less than zero and decreases toward -1 as this distance increases. The relative echo flux for the magnetopause thus decreases by less than $1/s^2$ as the standoff distance varies, becoming 2.1×10^{-16} m^{-2} for an 8-R_E magnetopause and 5.4×10^{-17} m^{-2} for a spherical, Earth-centered 12 R_E magnetopause. In addition, when the actual center of curvature lies sufficiently outside the Earth and plasmasphere to avoid shadowing, such magnetopause echoes should also be detectable from the night hemisphere, outside the focal distance on the opposite side of the Earth at echo distances of roughly 16 R_E and with relative fluxes of about 5×10^{-18} m^{-2}.

Ripples at the magnetopause will affect these fluxes, as discussed in Appendix A, as will also the gradually increasing radius of curvature along the flanks of the magnetosphere. Such ripples and changing curvature, on the other hand, will often cause multiple echoes from different directions, and because of the way a sounder works, as discussed in section 5.4, such echoes are easily distinguished by their different delays and doppler shifts. It should therefore sometimes be possible to measure the approximate shape and distance of the magnetopause in only a few seconds at a single fixed frequency, and thereby produce complete short-time-scale three-dimensional maps of the front surface of the magnetosphere.

2.9. Plasmapause

Although the actual size and shape of the plasmapause could be quite different, as discussed by *Carpenter* [1995], the plasmapause will be modeled by an **L** = 4 dipole **L** shell as shown in Figure 5. Its shape can then be represented by

$$r = L \cos^2 \lambda_m \quad (10)$$

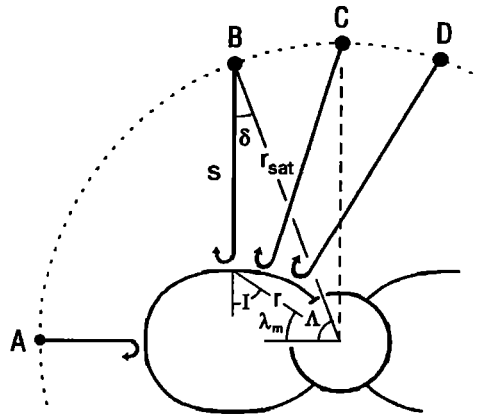

Figure 5. Plasmapause echo geometry for sounder positions **A**, **B**, **C**, and **D**.

where **r** is the radial distance and λ_m is the magnetic latitude. The magnetic dip angle **I** is then

$$\tan I = 2 \tan \lambda_m \tag{11}$$

In terms of **I** and **r**, as shown in Appendix B, the plasmapause radius of curvature in the magnetic meridian is

$$R_1 = \frac{2r}{(3\cos^2 I + 1)\cos I} \tag{12}$$

and in the echo plane perpendicular to the magnetic meridian, the azimuthal radius of curvature is found to be

$$R_2 = \frac{2r\cos I}{3\cos^2 I - 1} \tag{13}$$

These radii of curvature are shown in Figure 6 as a function of magnetic latitude. At the equator, $R_1 = 2\ R_E$ and $R_2 = 4\ R_E$. Both then increase with latitude, with R_2 becoming infinite at a magnetic latitude of 35.3°, corresponding to position **B** in Figure 5 where the dip angle

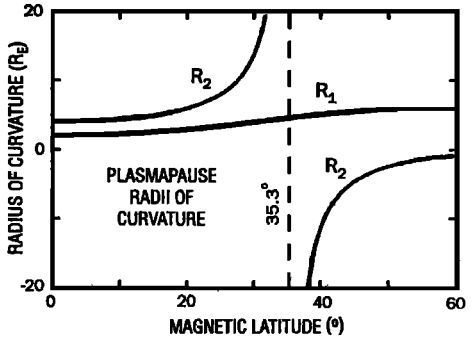

Figure 6. Plasmapause radii of curvature R_1 in the magnetic meridian and R_2 perpendicular to that meridian.

equals the magnetic colatitude. Beyond this point the azimuthal curvature then switches sign, like that of the inside of a donut hole, becoming concave at higher latitudes and causing focusing along the polar axis of the plasmasphere as discussed below.

From the law of sines for the triangle formed by **s**, r_{sat}, and **r** in Figure 5, where **s** is the echo distance and r_{sat} is the sounder geocentric altitude, the echo distance can then be expressed as

$$s = \frac{\sin(I - \delta)}{\sin I} r_{sat} \tag{14}$$

where $\delta = I + \lambda_m - \Lambda$ and Λ is the satellite magnetic latitude. The angle δ is then

$$\delta = \sin^{-1}\left(\frac{r}{r_{sat}} \sin I\right) \tag{15}$$

The relative echo flux for the plasmapause was then calculated as follows. **r**, **I**, R_1, and R_2 were first calculated for a given magnetic latitude from Equations (10) to (13), δ was then calculated from Equation (15) for $r_{sat} = 6\ R_E$, and **s** was calculated from this result and Equation (14). The relative echo flux was then calculated from Equation (9) and plotted against $\Lambda = I + \lambda - \delta$ in Figure 7, where points **A** through **D** correspond to the positions **A** through **D** in Figure 5.

As shown in Figure 7, the relative echo flux for the plasmapause decreases from about 4.1 x 10^{-17} m^{-2} at the equator to a minimum of about 1.6 x 10^{-17} m^{-2} just slightly poleward of position **B** in Figure 5. This decrease, which is caused by the increased distance, is partially offset by the decreased defocusing which occurs as the radii of curvature increase with latitude. The flux then increases sharply to point **C** where the concave azimuthal curvature at high latitudes causes focusing along the polar axis. For an exactly symmetrical plasmapause, this focusing results from echoes coming from a continuous ring around the pole, and for a plasmapause which is not exactly symmetrical, it turns into a cone of focused echoes at the actual azimuthal center of curvature of the plasmapause. The echoes from **C** to **D** then correspond to echoes from the opposite side of the pole and the dashed curve corresponds to echoes for sounder positions which are the left-to-right mirror image of those in Figure 5. Two echoes, and perhaps more for an odd-shaped plasmapause, should thus occur within about 30° of the polar axis, coming from high and low altitudes on opposite sides of the plasmasphere. The symmetry of the plasmapause, for example, could easily be measured from such echoes, since they would be detected almost simultaneously and can easily be distinguished by their different direction, delay, and doppler shift.

2.10. Plasmasphere

Although the density contours of the plasmapause tend to follow the magnetic field, those inside the plasma-

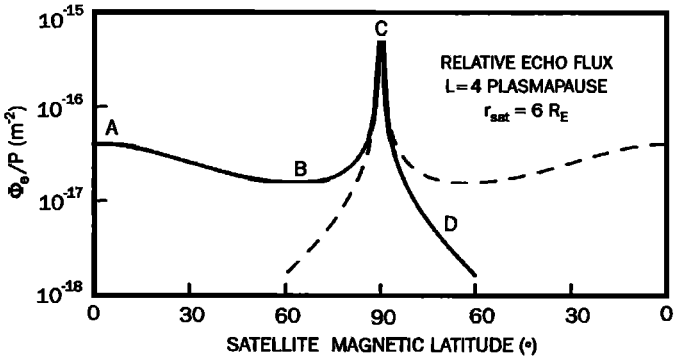

Figure 7. Relative echo flux for the plasmapause, where **A** thru **D** pertain to Figure 5 and the dashed curves pertain to the same positions measured from the other side of the plasmasphere.

sphere take on a different shape because of diffusive equilibrium, becoming approximately Earth-centered spheres as shown in Figure 1. The echo direction thus shifts as the echo point moves into the plasmasphere, becoming almost radial except for wave refraction at the plasmapause. As a result, these echoes will be observed only at relatively low satellite magnetic latitudes, below about 60°.

The density of the plasmasphere at the equator, according to *Carpenter and Anderson* [1992] and *Carpenter et al.* [1993], decreases logarithmically with geocentric altitude from about 2000 cm^{-3} at **L** = 2 to 400 cm^{-3} at **L** = 4, and the radii of curvature of these density contours should approximately equal the geocentric altitude at the point of reflection. The resulting echo flux for a sounder at 6 R_E then becomes that shown in Figure 8, decreasing from about 5.4 x 10^{-17} m^{-2} at 180 kHz, for echoes from just inside the plasmapause, to 3.4 x 10^{-18} at 400 kHz corresponding to echoes from deep inside the plasmasphere at an altitude of about 6000 km.

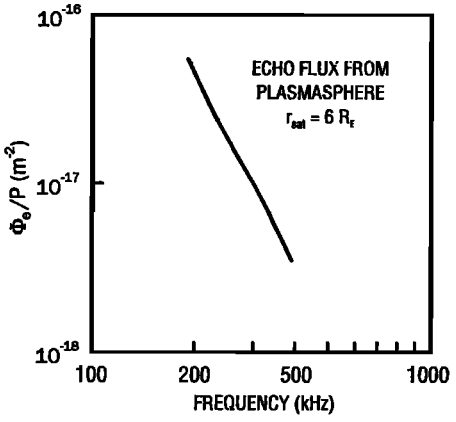

Figure 8. Relative echo flux for the plasmasphere according to the model of *Carpenter and Anderson* [1992].

2.11. Flux Summary

The relative echo fluxes for the magnetopause, plasmapause, and plasmasphere, for a sounder at 6 R_E, are listed in Table 1, along with the approximate frequency and echo distance for these targets. Magnetopause echoes can thus be characterized by a relative flux of 8.5 x 10^{-17} m^{-2}, corresponding to a 10-R_E Earth-centered magnetopause, and those of the plasmapause by a relative flux of 1.6 x 10^{-17} m^{-2} corresponding to the minimum in Figure 7 at a satellite magnetic latitude of 70°. Along with Figure 8 for the plasmasphere, these will then be used to calculate the echo strengths and signal-to-noise ratios for these targets in sections 3.3 and 5.3.

Other structures will also be detected which are of major interest to magnetospheric research. The cusp and cavity in Figure 1, for example, should be detectable at distances of up to about an Earth radius as the sounder passes near and inside these features, respectively. The plasmapause outliers of *Chappell* [1974] and *Carpenter* [1995] should also be detectable as additional echoes in the evening sector and sometimes also locally as the satellite passes directly through these features. The magnetopause boundary layer may also be detectable as a low-frequency density step just inside the magnetopause and the near-Earth plasma sheet on the other side of the

Table 1. Relative Echo Flux, Plasma Frequency, and Distance of Sounding Targets in the Magnetosphere

Target	Relative Flux, 10^{-17} m^{-2}	Frequency, kHz	Distance, R_E
Magnetopause	5.4 - 21	30 - 150	2 - 6
Plasmapause	1.6 - 4.1	30 - 180	2 - 5
Plasmasphere	0.3 - 5.4	180 - 400	2 - 4

Earth could also be mapped by a sounder satellite as it passes through that region. Although similar interesting studies could also be carried out for the echoes from each of these targets, this paper will focus only on the magnetopause, plasmapause, and plasmasphere.

3. Pulse Transmission

In order to determine the actual echo flux, it is necessary to multiply these relative fluxes by the effective radiated power of the sounder. This then requires analyzing the power which can be radiated by the two spin-plane antennas as a function of frequency.

3.1. Equivalent Circuit

The equivalent circuit for pulse transmission is shown in Figure 9, where R_a is the radiation resistance, X_a is the antenna reactance, and V_a is the root-mean-square (rms) voltage at the root of the transmitting antenna. The antenna current is thus

$$I_a = \frac{V_a}{\sqrt{R_a^2 + X_a^2}} \tag{16}$$

The power P_t which is delivered to the radiation resistance, and hence radiated by the antenna, is therefore

$$P_t = I_a^2 R_a = \frac{R_a V_a^2}{R_a^2 + X_a^2} \tag{17}$$

According to *Jordan* [1950], the radiation resistance and capacitive reactance, in ohms, of a short dipole antenna of length $L_a \ll \lambda$, are given by

$$R_a = 20\pi^2 \left(\frac{L_a}{\lambda}\right)^2 \tag{18}$$

and

$$X_a = \frac{120}{\pi}\left[\ln(L_a/2a) - 1\right]\left(\frac{\lambda}{L_a}\right) \tag{19}$$

where $\lambda = c/f$ is the wavelength, L_a is the tip-to-tip antenna length, and a is its radius. These impedances are shown in Figure 10 as a function of frequency for a 500 m wire antenna which is 1 mm in diameter, along with their schematic behavior at the higher frequencies where these equations are no longer valid.

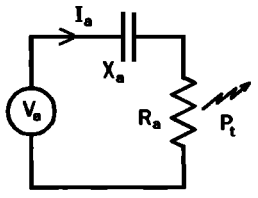

Figure 9. Equivalent circuit for pulse transmission.

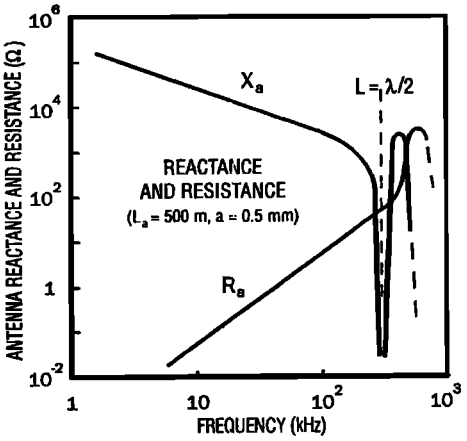

Figure 10. Reactance and radiation resistance for a 500-m dipole antenna (schematic).

As discussed by *Balmain* [1964] and *Franklin and Maclean* [1969], the nearby plasma will affect these impedances at frequencies near the local plasma and cyclotron frequencies. Outside the plasmapause, however, for distant targets like the magnetopause and plasmasphere, such effects can be neglected since the sounding frequency is significantly higher than both of these frequencies, whereas for the short-range echoes at lower frequencies where these effects are important, echo signal strength is not expected to be a problem.

3.2. Radiated Power

As shown in Figure 10, the radiation resistance is quite low at low frequencies, and the antenna reactance is quite large, increasing with decreasing frequency. This combination then severely limits the power which can be radiated at low frequencies. At 30 kHz, for example, where the radiation resistance and reactance are approximately 0.5 Ω and 9000 Ω, respectively, the antenna current for a voltage of V_a = 3000 V is only about 300 mA and the radiated power is then only about 50 mW. High voltages are therefore necessary to radiate significant power at low frequencies, and according to Equations (17-19) for $X_a \gg R_a$, the power which is radiated by the long spin-plane antennas such frequencies is then

$$P_t \approx \frac{R_a V_a^2}{X_a^2} = \frac{0.135\,(L_a/\lambda)^4 V_{max}^2}{[\ln(L_a/2a) - 1]^2} \tag{20}$$

where L_a is the transmitting antenna length and V_{max} is the rms transmitter voltage at the root of the antenna. The radiated power thus decreases as the fourth power of the frequency, and the power which can be radiated for L_a = 500 m, a = 0.5 mm, V_{max} = 3 kV, and a maximum transmitter power of P_{max} = 10 W is shown in Figure 11.

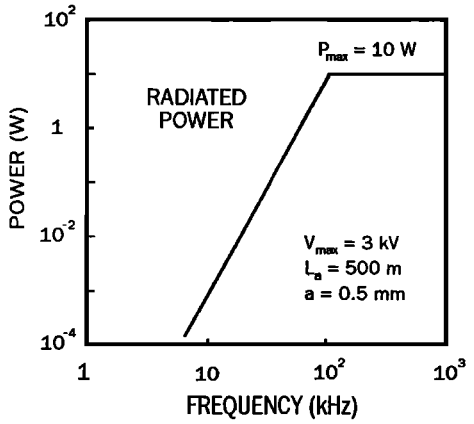

Figure 11. Radiated power for a 10-W, 3-kV transmitter with a 500-m antenna.

According to Equation (20) the breakpoint between voltage and power limiting occurs at

$$f_b = \frac{1.65\,c}{L_a}\sqrt{\frac{\ln(L_a/2a)-1}{V_{max}}}\sqrt[4]{P_{max}} \qquad (21)$$

which is 112 kHz as shown in Figure 11 for a 500-m antenna, and 140 kHz for a 400-m antenna. According to Equation (21), the low-frequency limit for a sounder thus varies inversely proportional to the antenna length times the square root of the transmitter voltage, whereas the corresponding high-frequency limit, which occurs above this breakpoint as a result of increased echo distance, is determined by the transmitter power.

The effective radiated power also depends on the antenna pattern and the polarization mismatch between the transmitted wave and the wave polarization of the plasma. The antenna gain of a short dipole, according to *Jordan* [1950], varies from about 50% gain to 25% loss at angles more than 45° to the axis of the antenna, and if the best antenna is used for transmission in a given direction, this factor can be neglected. At low densities where both waves are circularly polarized as discussed by *Allis et al.* [1963, chap. 4], the polarization loss for a linear antenna is 3 dB. This loss, however, can be compensated for by transmitting the appropriate sense of circular polarization, and except in the spin plane where this loss is still 3 dB, the polarization loss can therefore also be neglected.

The resulting echo power flux for the magnetopause, plasmapause, and plasmasphere is shown in Figure 12, along with the reception thresholds determined below. The corresponding electric field strength, which is given by $\mathbf{E}^2 = 377\,\Phi_e$ where $\mathbf{E}$ is the field strength in volts per meter and Φ_e is the echo power flux in watts per meter squared, is shown by the scale on the right side of this figure.

4. Reception

The threshold for reception is determined by the internal and external noise, and it is therefore necessary to identify these noise sources and compare their equivalent noise fluxes to those in Figure 12.

4.1. Equivalent Circuit

The equivalent circuit for reception is shown in Figure 13, where $\mathbf{R}_a$ is the radiation resistance, $\mathbf{X}_a$ is the antenna

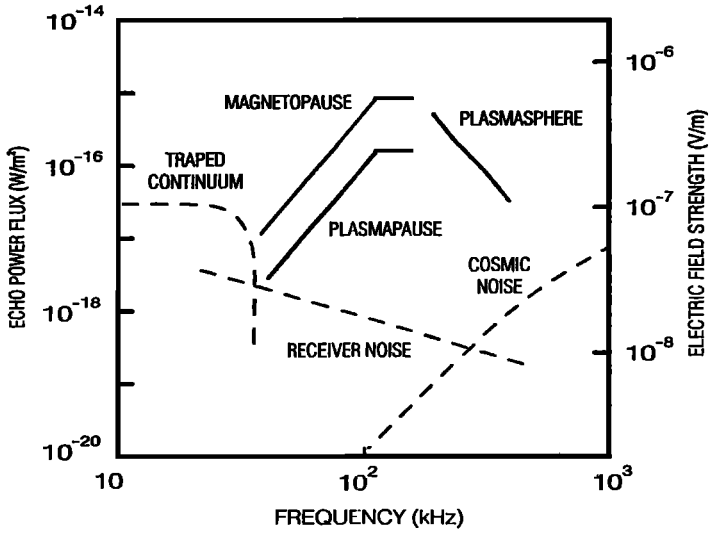

Figure 12. Echo flux and reception thresholds for a bandwidth of 300 Hz and the cosmic noise measurements of *Bougeret et al.* [1984].

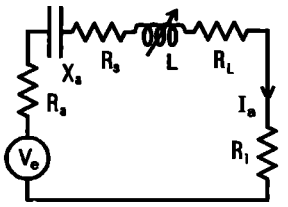

Figure 13. Equivalent circuit for reception, where R_a is the ohmic resistance of the antenna, R_l is the receiver input impedance and L is a series inductor which has been included for antenna tuning.

reactance, R_a is the ohmic resistance of the antenna, R_l is the receiver input impedance, L is a series inductance to tune the antenna, and R_L is the effective series resistance of that inductor. According to *Jordan* [1950, chap. 12], the echo signal appears as a voltage

$$V_e = \sqrt{\frac{\lambda^2}{4\pi} R_a \Phi_e} \tag{22}$$

in series with the antenna, where λ is the wavelength, R_a is the radiation resistance, and Φ_e is the incoming echo power flux. The echo power that reaches the receiver then becomes

$$P_r = I_a^2 R_l = \frac{V_e^2 R_l}{Z_a^2} = \frac{\lambda^2 \Phi_e R_a R_l}{4\pi Z_a^2} \tag{23}$$

where

$$Z_a^2 = (\omega L - X_a)^2 + (R_a + R_s + R_L + R_l)^2 \tag{24}$$

is the total series impedance of the antenna circuit and $\omega = 2\pi f$ is the angular frequency.

4.2. Equivalent Receiver Noise Flux

The factor limiting reception at intermediate frequencies is the thermal noise power of the receiver, given by

$$P_n = q\, k\, T\, \Delta f \tag{25}$$

where q is its noise figure (typically 3 for a good design), T is the Kelvin temperature, $k = 1.38 \times 10^{-23}$ J/K is Boltzmann's constant, and Δf is the receiver bandwidth [*Bennett*, 1960]. In order to compare this noise power to the echo power flux it is convenient to convert the former into an equivalent noise flux by equating P_n to P_r in Equation (23) and solving for $\Phi_n = \Phi_e$:

$$\Phi_n = \frac{q\, k T \Delta f}{5\pi L_a^2} \left[\frac{Z_a^2}{R_l}\right] \tag{26}$$

where L_a is the receiving antenna length and R_a has been eliminated using Equation (18).

4.3. Antenna Tuning and Impedance Matching

In order to minimize the equivalent receiver noise flux, L and R_l are adjusted to minimize Z_a^2/R_l, requiring an inductance of

$$L = \frac{X_a}{\omega} = \frac{60\, c\, [\ln(L_a/2a) - 1]}{\pi^2 f^2 L_a} \tag{27}$$

and a receiver input impedance of

$$R_l = R_a + R_s + R_L \tag{28}$$

where

$$R_L = \frac{\omega L}{Q} = \frac{120\, c\, [\ln(L_a/2a) - 1]}{Q \pi f L_a} \tag{29}$$

is the effective series resistance of this inductor and Q is its Q of this inductor, assumed to be about 100. This then gives $Z_a^2/R_l = 4(R_a+R_s+R_L)$ and the equivalent receiver noise flux then becomes

$$\Phi_n = \frac{4\, q\, k T \Delta f (R_a + R_s + R_L)}{5\pi L_a^2} \tag{30}$$

The inductance which is required for tuning thus increases inversely with the square of the frequency, and this would be implemented using a tapped inductor which is adjusted under computer control to maximize the received signal. For a 500-m wire spin-plane antenna with a = 0.5 mm, this inductance varies from about 5 mH at 100 kHz to 50 mH at 30 kHz, having an effective internal resistance for Q = 100 which decreases with frequency from about 90 Ω at 30 kHz to 30 Ω at 100 kHz. On the other hand, for the 10-m to 20-m spin-axis antenna, with a = 1.25 cm, this inductance could be as large as 0.5 to 1.1 H at 30 kHz with an effective resistance as large as 1000 to 2000 Ω.

Prototype tuning circuits for a 10 m spin-axis antenna have been developed at the University of Massachusetts Lowell by K. Bibl. These circuits use voltage-controlled capacitors for fine tuning and ceramic cup-core inductors weighing about 100 g. It is intended to select inductor taps for different frequency bands and use automatic tuning within these bands in order to compensate for changes in the antenna impedance caused by the plasma.

For the long spin-plane antennas, R_a is large compared to R_s and should be roughly 50 Ω. The required input impedance for this antenna is thus in the range of 80 to 140 Ω. On the other hand, for the short antenna R_a and R_s are both negligible compared to the effective internal resistance of the inductor, and the input impedance then becomes

$$R_l = R_L = X_a / Q \tag{31}$$

whereupon Equation (28) becomes

$$\Phi_n = \frac{96\,c\,q\,k\,T\Delta f\,[\ln(L_a/2a) - 1]}{\pi^2 f\,Q\,L_a^3} \qquad (32)$$

According to Equation (28) the receiver input impedance for the short antenna varies with frequency, decreasing from about 2000 Ω at 30 kHz to 200 Ω at 300 kHz, and it is therefore necessary to adjust this impedance for optimum reception at different frequencies.

For an untuned antenna the corresponding input impedance would have been $R_i = X_a$, requiring a high-impedance preamplifier, whereas for a tuned antenna this becomes X_a/Q, as specified by Equation (31). The required input impedance is thus less by a factor of Q. Also, the quantity Z_a^2/R_i in Equation (26), which would have been $2X_a$ for an untuned antenna, becomes $4X_a/Q$ for a tuned and matched antenna, thus yielding an equivalent receiver noise flux which is lower by a factor of $Q/2 = 50$, or 17 dB. A Q of 100, moreover, is also appropriate for receiving with a 300 Hz bandwidth at 30 kHz.

According to Equation (30), for $q = 3$, $T = 300°$ K, $\Delta f = 300$ Hz, $R_a \approx 0$, $R_s = 50$ Ω, and $R_L = 90$ Ω, the noise flux for an $L_a = 500$-m spin-plane antenna at 30 kHz should be about 5.3×10^{-22} W/m^2. For a 10 m spin-axis antenna with $a = 1.25$ cm and $Q = 100$, this noise flux, according to Equation (32), varies from 3.3×10^{-17} W/m^2 at 30 kHz to 3.3×10^{-18} W/m^2 at 300 kHz, whereas for a 20 m antenna, this noise flux varies from 2.6×10^{-18} W/m^2 at 30 kHz to 2.6×10^{-19} W/m^2 at 300 kHz.

Although much weaker signals can be detected with the long spin-plane antennas, it is the short antenna which determines the threshold for measuring echo directions out of the spin plane, as discussed in section 6. The noise flux of this antenna is therefore adopted as the reception threshold for a sounder, as shown in Figure 12 for a 20 m spin axis antenna. The effect of this choice for the spin-axis antenna length is discussed in section 8 and the corresponding signal-to-noise ratio after digital integration is discussed in section 5.

4.4. External Noise

External noise includes cosmic noise, solar noise, trapped and escaping continuum, and auroral kilometric radiation (AKR). Cosmic noise, which is smooth and always present, establishes the noise floor for radio sounding, as shown in Figure 12 for a bandwidth of 300 Hz from the measurements of *Bougeret et al.* [1984].

Solar noise at low frequencies consists primarily of short-term type III solar radio bursts lasting a few tens of minutes with spectral fluxes as much as four or more orders of magnitude stronger than cosmic noise, along with relatively infrequent, longer-term noise storms having average fluxes which are only about ten times greater, as shown in Figure 4 of *Bougeret et al.* [1984]. Although the former will prevent sounding intermittently, on time scales of up to an hour during solar maximum, the latter will decrease the signal-to-noise ratio by only about a factor of 3 for periods of a day or two during such storms. Since both are relatively rare, however, neither is considered a very serious problem for radio sounding.

Although often much stronger and originating in the auroral zone at frequencies of 50 to a few hundred kilohertz, AKR is found to consist of discrete components with spectral spacings of 5 to 10 kHz and bandwidths sometimes as narrow as only about 5 Hz [*Gurnett and Anderson*, 1981; *Benson et al.*, 1988; *Baumback and Calvert*, 1987]. These discrete components are also usually stable over the few seconds which is required for sounding, as shown in Figures 6, 7, and 8 of *Gurnett and Anderson* [1981]. It should therefore be feasible to eliminate most if not all of the interference from AKR by measuring the noise level first and sounding in between these adjacent discrete frequencies. This technique, which is now used routinely by modern digital ionosondes to reject interference from broadcast stations, is found to work extremely well and to virtually eliminate all such interference [*Reinisch*, 1986; *Reinisch et al.*, 1992]. Moreover, since the frequency occupancy of AKR is generally less than of a crowded shortwave broadcast band, and also since it lacks the variable sidebands of commercial broadcast stations, it should work even better for AKR. In addition, since AKR is intermittent, extending below 70 kHz less than half of the time while it is active at higher frequencies, as shown in Figure 5 of *Gurnett and Anderson* [1981], useful observations should still be possible half or more of the time even if all such interference cannot be eliminated by this technique.

Terrestrial continuum is generated near the equator at the plasmapause [*Gurnett et al.*, 1988] and originates as discrete emissions at the plasma frequency which can also be eliminated by the same technique [*Kurth et al.*, 1981, *Kurth*, 1982]. However, at frequencies below the peak magnetopause plasma frequency in the distant tail, these emissions become trapped inside the magnetosphere and consist of many overlapping discrete components which are often too smooth in frequency to be eliminated by this method [see *Kurth et al.*, 1981, Figures 1 and 2]. Such trapped continuum, as shown in Figure 12, typically occurs below about 30 to 40 kHz at spectral flux levels ranging from 10^{-20} to 10^{-18} W/m^{2}Hz [R. R. Anderson, private communication, 1994]. However, since it always occurs at or below the peak plasma frequency of the plasmapause and front-side magnetopause, it should thus rarely if ever interfere with detecting these targets or with measuring the plasma density at higher frequencies within the plasmasphere.

Other emissions in the whistler mode which occur below the plasma frequency obviously cannot interfere with sounding, and auroral Z mode emissions [e.g., *Hash-*

imoto and Calvert, 1990] will affect sounding only at relatively low altitudes in the auroral zone at frequencies below the local upper-hybrid resonance frequency. The plasma resonances of *Etcheto and Bloch* [1978], which are excited locally by the sounder transmitter and last for only a few tens of milliseconds at specific frequencies, should also not significantly interfere with sounding and in fact will be quite useful for determining the local density and magnetic field. Ducted echoes propagating along the magnetic field are also not considered interference, since they are easily distinguished by their different delays and directions, and these echoes will also be useful for determining the density distribution along the magnetic field, as discussed by *Dyson and Benson* [1978] and *Calvert* [1981b].

Except for intermittent interference by solar noise, AKR, and escaping continuum, the major external noise sources which affect radio sounding are therefore cosmic noise at high frequencies and trapped continuum at low frequencies, as shown in Figure 12.

5. Digital Integration

In order to measure echo directions it is necessary to detect echoes with an adequate signal-to-noise ratio. This signal-to-noise ratio, which equals the square root of the power ratio between the echoes and noise in Figure 12, can be improved using pulse compression and spectral integration, as discussed by *Reinisch et al.* [1992] and *Haines* [1994] and summarized as follows.

5.1. Pulse Compression

Pulse compression involves transmitting a phase-modulated pulse consisting of **n** "chips" of length **t**, each chip being equivalent to a separate sounder pulse. The resulting echoes are then correlated with the original modulation pattern, as shown in Figure 14, producing a compressed echo signal of amplitude **nS** which is the coherent sum of the **n** individual echo chips of amplitudes **S**. The accompanying noise adds incoherently, however, producing a noise signal which equals the square root of **n** times the noise **N** of a single chip. Equivalent to averaging **n** repeated measurements, this yields an increase in the signal-to-noise ratio by the square root of **n**.

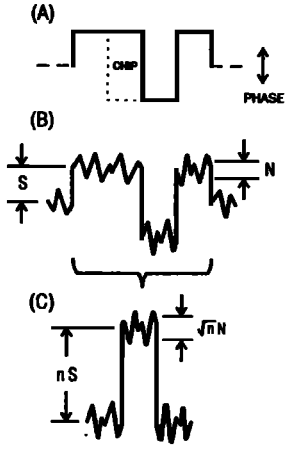

Figure 14. Pulse compression, in which a phase-coded pulse (**A**) produces echoes (**B**), of amplitude **S** and noise **N**, which are correlated with the original chip pattern (**C**) to improve the signal-to-noise ratio.

This procedure can be carried out for each complete overlapping sequence of **n** chips which are received after a transmitter pulse, thus yielding echo measurements at the delay interval of a single chip. The first complete echo pattern, which starts immediately after the transmitter pulse, then corresponds to an echo delay of **n** times **t**, where **t** is the time of a single chip. The next pattern, which overlaps the first and is displaced later by a single chip, then corresponds to an echo delay of **(n+1)t**, the third is displaced by two chips, corresponding to an echo delay of **(n+2)t**, and so forth.

This technique, on the other hand, causes a dead time during transmission, during which echoes cannot be received, and this is the principal disadvantage of this method. Using a 53-ms pulse consisting of sixteen 3.3-ms chips, for example, yields a factor of 4 improvement in the signal-to-noise ratio at the expense of not being able to receive echoes during the first 53 ms (or 1.2 R_E) of echo delay. Pulse compression therefore sacrifices nearby echoes in exchange for a better signal-to-noise-ratio. In the magnetosphere where the target distances are usually a few Earth radii, values for **n** of 8 to 32 can thus be used to improve the signal-to-noise-ratio by a factor of 2.8 to 5.6 at the expense of not being able to receive nearby echoes at distances of up to 0.6 to 4.8 R_E, respectively.

5.2. Spectral Integration

Spectral integration requires transmitting multiple pulses and spectrum analyzing the echoes which are received at the same delay after each pulse, as shown in Figure 15. The spectrum analysis of **m** consecutive samples is equivalent to averaging **m** repeated measurements having the same phase shift between adjacent samples. Consequently, for echoes having a specific Doppler shift or progressive phase change caused by changing plasma conditions, the echoes for all **m** pulses add coherently into a single channel, as shown in Figure 15B, producing a spectral component equal to **m** times **S** and noise which is proportional to the square root of **m** times **N**, where **N** and **S** are the noise and echo amplitudes. As with pulse compression, this then yields a signal-to-noise-ratio improvement equal to the square root of **m**.

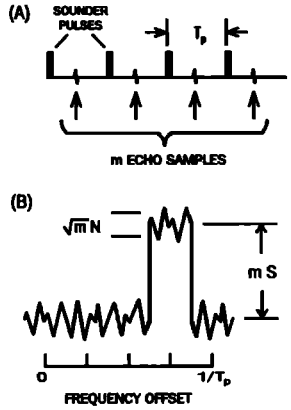

Figure 15. Spectral integration, in which multiple echoes at the same delay (**A**) are spectrum analyzed (**B**) to improve the signal-to-noise ratio.

5.3 Combined Pulse Compression and Spectral Integration

Pulse compression and spectral integration are thus complementary techniques in the time and frequency domains, and when both are used the resulting signal-to-noise ratio becomes

$$S/N = \sqrt{mn}\, S/N_o \qquad (33)$$

where S/N_o is the raw signal-to-noise ratio from Figure 12. This requires transmitting **m** phase-coded pulses of **n** chips each and performing a combined correlation and spectral analysis of the resulting echoes. Using **m** = 8 and **n** = 16, for example, yields an overall improvement of about 11.3, or 21 dB, which is then equivalent to transmitting 128 times the actual radiated power. The resulting signal-to-noise ratios for these values of **m** and **n** are shown in Figure 16.

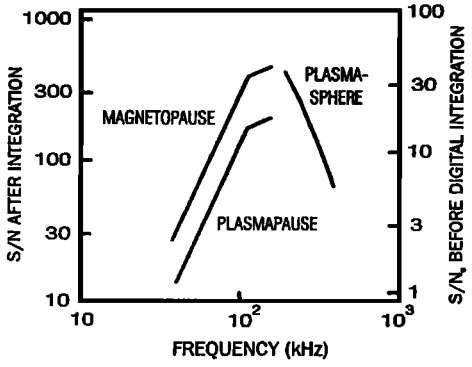

Figure 16. Signal-to-noise ratios for Figure 12, before (S/N_o) and after (S/N) sixteen-chip pulse compression and eight-point spectral integration.

5.4. Typical Measurement

In order to illustrate how this works, the following example will show how such echoes would be analyzed using eight-point spectral integration and sixteen-chip pulse compression, for a chip length of 3.3 ms and a pulse repetition period of 0.5 s. This requires transmitting eight 53-ms coded pulses at 0.5-s intervals and sampling the echo signals which are received at 3.3-ms intervals during the remaining 500-53 = 447 ms after each pulse. This then yields 447/3.3 = 135 consecutive samples after each pulse, of which 120 correspond to complete echo patterns, since the last 15 samples before the next pulse correspond to an incomplete pattern of the 16-chip coded pulse. These 120 patterns, corresponding to echo delays of 53 to 53+120x3.3 = 449 ms, would then be correlated with the transmitted pattern in order to produce 120 compressed echo signals for each pulse and a total of 8x120 = 960 compressed signals for the eight-pulse sequence. These echo signals are then spectrum analyzed, eight at a time for the same delay after each pulse, producing 120 spectra consisting of 120x8 = 960 complex spectral amplitudes representing the echo amplitude and phase at 8 spectral offsets and 120 delays. This calculation would be carried out for each of the three antennas, producing 3x960 = 2880 measurements from which the echo amplitude and direction can then be computed separately for each delay and spectral offset. The result is eight measurements of echo amplitude and direction for each of 120 delays at free-space echo distances of 53/43 = 1.2 R_E to 449/43 = 10.4 R_E.

A four-second measurement thus requires 120x3x8 = 2880 sixteen-chip pulse correlations and 3x120 = 360 eight-point spectral integrations. Using modern digital computers, however, these calculations can be carried out during the next measurement, and the data rate, assuming that 8 bits are used to represent the three quantities representing the echo amplitude and direction, would be 3x960x8 = 23,040 bits in 4 s, or 5760 bit/s. With data compression, however, these data can be compressed by a factor of five or more, thus yielding an actual data rate of about 1 kbit/s.

5.5. Doppler Spectrum

The penalty of having to transmit multiple pulses for spectral integration, however, is partially offset by the added benefit of being able to measure the Doppler shift caused by satellite motion. For **m** pulses and a pulse repetition period of T_p, spectrum analysis yields **m** spectral amplitudes as a function of frequency over a frequency interval of $1/T_p$ in steps of $1/mT_p$. For T_p = 0.5 sec and **m** = 8 it thus yields eight measurements over a ±1-Hz interval in steps of 0.25 Hz, and this turns out to be ideal for measuring the Doppler shift of satellite mo-

tion, since the line-of-sight velocity corresponding to a Doppler shift of Δf_d is

$$v_d = \frac{c}{2}\frac{\Delta f_d}{f} \tag{34}$$

and this then corresponds to line-of-sight velocities of ±1.5 km/s at 100 kHz, in steps of 400 m/s. For a satellite velocity of 1.5 km/s the eight spectral channels would then correspond to eight different directions with respect to the satellite velocity vector, in equal cosine intervals from 0° to 180°. The echo direction can thus be determined to within about $\cos^{-1}0.75 = 41°$ in the forward and backward directions, and to within $\cos^{-1}0.25 = 15°$ at right angles to the satellite velocity. Although not clearly adequate for measuring echo directions, as discussed below, measuring these Doppler shifts is useful for distinguishing multiple echoes from different directions, and also for determining the sense of propagation along the echo direction in order to resolve the sense ambiguity of measuring echo directions with electric antennas.

6. Echo Direction

Although in ionospheric sounding the echo paths were generally almost vertical because of horizontal stratification, in the magnetosphere echoes can arrive from any direction and it is therefore necessary to measure their direction of arrival.

6.1. Direction Measurement

Since the propagation direction is approximately perpendicular to the so-called E plane of the wave, as shown in Figure 17 [see *Allis et al.*, 1963, chap. 4], it is sufficient to measure echo directions from three orthogonal components of the wave electric field. This measurement requires coherent reception using three orthogonal antennas and yields three pairs of in-phase and quadrature echo signals representing the electric vector at orthogonal directions in the E plane, as shown in Figure 17. The echo direction can then be determined from the vector cross product of these in-phase and quadrature signals, yielding three quantities equal to the wave amplitude times the direction cosines of the E plane normal.

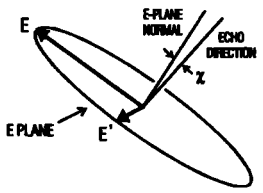

Figure 17. Wave E plane determined from the in-phase and quadrature electric field vectors **E** and **E'**, where χ is the wave-normal deviation angle of *Allis et al.* [1963].

Except for the extraordinary wave near cutoff for propagation almost exactly perpendicular to the magnetic field, the E plane normal represents a good approximation for the wave normal direction, as discussed by *Allis et al.* [1963, chap. 4], although under certain circumstances it will be necessary to correct for the wave normal deviation angle χ between these two directions, as shown in Figure 17. In addition, it will also sometimes be necessary to correct for the difference between the wave normal and ray directions, since it is actually the latter which is the desired echo direction, and these two can also sometimes be different, as discussed by *Calvert* [1966]. Such corrections, however, are well understood and can be determined from the local density and magnetic field determined by the sounder. There is also an ambiguity in the echo direction measured by this technique, since the wave electric field is the same for opposite propagation directions. This ambiguity, however, can be resolved either by measuring the Doppler shift or by analyzing the systematic changes of echo direction as a function of satellite motion.

6.2. Angular Precision

As shown in Figure 18, the electric vectors **E** which are used to measure the echo direction will be accompanied by a vector noise signal **ΔE**, equal in magnitude to the electric field divided by the signal-to-noise ratio. This introduces an angular uncertainty of ±**ΔE**/**E** in the direction of the electric field, and hence also in the echo directions measured from these fields. The full-width angular precision $\Delta\theta$ of a sounder thus equals twice the reciprocal signal-to-noise ratio:

$$\Delta\theta = 2\frac{\Delta E}{E} = \frac{2}{S/N} \tag{35}$$

A signal-to-noise ratio of 100 then corresponds to a full-width angular precision of 0.02 rad, or about 1°, and for the signal-to-noise ratios in Figure 16, this occurs at frequencies above 50 kHz for the magnetopause, above 75 kHz for the plasmapause, and below 350 kHz for the plasmasphere. The best angular precision for these signal-to-noise ratios is thus about 0.4°, corresponding to the signal-to-noise ratios of about 300 between about 80 and 230 kHz for the magnetopause and plasmasphere.

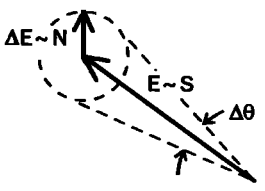

Figure 18. Angular uncertainty $\Delta\theta$ for a vector signal **S** and noise **N**.

6.3. Spatial Resolution

As shown in Figure 19, the transverse resolution of a sounder at a distance s then becomes

$$\Delta s_{\perp} = s\,\Delta\theta = \frac{2\,s}{S/N} \tag{36}$$

The transverse spatial resolution at a distance of 4 R_E for a signal-to-noise ratio of 100 is thus about 500 km. The corresponding range resolution, on the other hand, is determined by the chip length t and the speed of light c:

$$\Delta s_{\parallel} = \frac{c\,t}{2} \tag{37}$$

A chip length of 3.3 ms thus yields 500 km range resolution, and this chip length was chosen to make these two the same.

6.4. Three-Dimensional Spatial Resolution

If the chip length is shortened to achieve finer range resolution, the receiver bandwidth must be increased proportionately in order to resolve adjacent chips in the returning echo signal. This, however, increases the noise and decreases the signal-to-noise ratio proportional to the square root of the receiver bandwidth. The resulting transverse spatial resolution thus increases proportional to the square root of the bandwidth:

$$\Delta s_{\perp} \sim \sqrt{\Delta f} \tag{38}$$

The range resolution, on the other hand, decreases proportional to the chip length and thus varies inversely with bandwidth:

$$\Delta s_{\parallel} \sim 1/\Delta f \tag{39}$$

The latter times the square of the former is therefore a constant for different pulse lengths, equal to

$$\Delta s_o^3 = \Delta s_{\parallel}\,\Delta s_{\perp}^2 \tag{40}$$

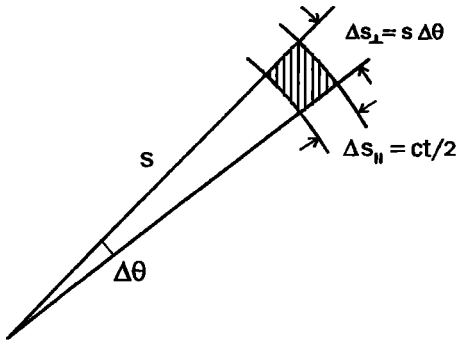

Figure 19. Transverse $\Delta s_{\perp}$ and longitudinal $\Delta s_{||}$ resolution for an angular resolution of $\Delta\theta$ and chip length t.

where Δs_o is the optimum three-dimensional spatial resolution.

This result is useful for determining an appropriate chip length and bandwidth for a given measurement, as follows. If the magnetopause distance is more important than its transverse structure, for example, one might use a chip length of 3.3/4 = 0.83 ms and a bandwidth of 4x300 = 1200 Hz in order to measure its distance with 500/4 = 125 km longitudinal resolution. Equation (40) then implies a transverse resolution of $(500^3/125)^{1/2}$ = 1000 km. On the other hand, if its transverse structure is more important, one might use a chip length of 4x 3.3 = 13.2 ms and a bandwidth of 300/4 = 75 Hz in order to measure with a longitudinal resolution of 4x500 = 2000 km and a transverse resolution of $(500^3/2000)^{1/2}$ = 250 km. In all three cases the product in Equation (40) remains the same, since 1000^2x125 = 250^2x2000 = (500 km)^3.

7. Precision and Temporal Resolution

7.1. Accuracy

The absolute distance and density accuracy of a sounder is determined from measurements of delay times and frequencies which can be measured to high precision with standard electronics. A sounder is therefore an absolute instrument and no precise calibration is required. In addition, this technique also measures the plasma frequency remotely without affecting the plasma which is being measured. The absolute accuracy of direction measurements, on the other hand, depends upon the precise phase calibration of the three antennas and their associated receivers.

7.2. Density Precision

The intrinsic density resolution of a sounder is determined by the receiver bandwidth according to Equation (1):

$$\frac{\Delta N_e}{N_e} = 2\,\frac{\Delta f}{f} \tag{41}$$

For a bandwidth of 300 Hz it thus varies from about 2% at 30 kHz to 0.2% at 300 kHz. The actual density precision, on the other hand, is determined by the frequency step between adjacent frequencies, requiring 5% frequency steps for 10% density resolution, and for a logarithmic frequency scan, $1/\log_{10}(1.05)$ = 47 frequency steps per decade.

7.3. True-Range Calculation

In order to calculate the density as a function of distance it is necessary to deconvolve the integral

$$t(f) = 2\int_0^x \frac{dx}{v_g(f, N_e(x), B(x), \theta(x))} \tag{42}$$

where t is the echo delay and v_g is the group velocity as a function of frequency, density, magnetic field, and direction.

The ray path retardation, which is defined by

$$\Delta x = c\frac{t}{2} - x \tag{43}$$

is then approximately $(c/v_g-1)x$ for abrupt targets like the magnetopause and plasmapause, and for such targets, where this quantity is roughly 5% of the distance and can presumably be determined to an accuracy of 20%, the absolute distance error at distances of 2 to 4 R_E should be only a few hundred kilometers. For a continuous target like the plasmasphere, on the other hand, inversion techniques like those which have been developed for the ionosphere by *Jackson* [1969a] and *Huang and Reinisch* [1982] would have to be used to calculate the density as a function of distance, yielding errors which are roughly 1% of the distance, according to *Jackson* [1969b]. In this case, also, since most of the ray path retardation occurs near reflection inside the plasmasphere over distances of 1-2 R_E, this should then also give absolute errors which are only a few hundred kilometers and hence comparable to the spatial resolution of the sounder.

7.4. Temporal Resolution

The density resolution of a sounder also determines its temporal resolution, as follows. For a logarithmic frequency sweep yielding constant fractional density resolution, the time which is required for sounding over the frequency range from f_1 to f_2 is then

$$t_{total} = \frac{m\,T_p \log(f_2/f_1)}{\log(1 + 0.5\,\Delta N/N)} \tag{44}$$

where $\Delta N/N$ is the desired density resolution, T_p is the pulse repetition period, and m is the number of pulses per frequency. The time which is required for sounding from 30 and 300 kHz with 10% density resolution and eight-point spectral integration, is therefore about 3 min.

Temporal resolution, on the other hand, can be traded off for finer spatial resolution, as follows. The optimum three-dimensional spatial resolution is proportional to the three-halves power of the transverse resolution according to Equation (40), the transverse resolution is inversely proportional to the signal-to-noise ratio according to Equation (35), and the signal-to-noise ratio is proportional to the square root of m according to Equation (33). The resulting three-dimensional spatial resolution thus varies inversely as the cube root of m, and hence also as the cube root of the measurement time, to wit:

$$t_{total} \sim m \sim \frac{1}{\Delta s_o^3} \tag{45}$$

A half-hour measurement using $m = 80$ instead of $m = 8$ could then be used to reduce the three-dimensional spatial resolution by the cube root of 10, or about a factor of 2.

8. Factors Affecting a Sounder Design

The main factors limiting the performance of a sounder are its antenna lengths, its transmitter power, and the antenna voltage during transmission. Long antennas are needed to transmit adequate power at low frequencies, and the 400 to 500 m spin-plane antennas were chosen to permit sounding at frequencies below about 100 kHz. One-kilometer wire antennas, on the other hand, have previously been deployed in space [*James*, 1991], and it is not inconceivable to contemplate antenna lengths of a few kilometers once the full benefits of radio sounding are appreciated by the magnetospheric research community.

The effect of using a longer transmitting antenna is to lower the breakpoint frequency in Equation (21), inversely proportional to its length, thus increasing the signal-to-noise ratios at low frequencies proportional to the square of this length, according to Equation (20). A 2 km length, for example, would permit using the full transmitter power down to about 28 kHz, consequently improving the signal-to-noise ratio at such frequencies by a factor of 16. Higher power, on the other hand, increases the signal-to-noise ratio only at the higher frequencies, so the only option for improving the low-frequency performance of a sounder is to increase its transmitter voltage. This voltage, however, is limited by cable insulation and the insulation of the deployment devices for these antennas. Although a voltage of 3 kV is feasible using standard techniques, if this could be increased to 10-30 kV by special insulation, the resulting signal-to-noise ratio, which is proportional to this voltage according to Equation (20), would increase by a factor of 3 to 10 without a longer antenna. At high frequencies, however, the only option is to increase transmitter power, since above the breakpoint in Equation (21) the radiated power is independent of both the antenna length and transmitter voltage.

At intermediate frequencies the length of the spin-axis antenna determines the threshold for measuring echo directions out of the spin plane. Since the signal-to-noise ratio decreases as the square root of the receiver noise flux according to Equation (32), it should thus increase proportional to the three-halves power of the spin-axis antenna length. The three-dimensional spatial resolution, on the other hand, is proportional to the two-thirds power of the angular resolution according to Equation (40). The resulting three-dimensional resolution therefore increases inversely proportional to this antenna length, thus becoming roughly 1000 km for a 10-meter spin-axis antenna.

A practical sounder, on the other hand, is dictated by other constraints, and it is considered feasible to make measurements which are of major importance to magneto-

spheric physics using a 10-W, 3-kV transmitter with antenna lengths as short as 400 m for the spin-plane antennas and 10 m for the spin-axis antenna. The effect of this choice, at frequencies below the breakpoint frequency, which now occurs at 140 kHz, is to reduce the signal-to-noise ratio inversely proportional to the square of the long antenna length and the three-halves power of short antenna length, according to Equations (20) and (36). The resulting three-dimensional spatial resolution, which varies inversely as the two-thirds power of the signal-to-noise ratio according to Equations (36) and (40), therefore varies inversely proportional to the short antenna length times the four-thirds power of the long antenna length:

$$\Delta s_o \sim \frac{1}{L_{short}\, L_{long}^{4/3}} \tag{46}$$

The spatial resolution for this configuration thus increases by a factor of 2.7 relative to that for antenna lengths of 500 m and 20 m, becoming 2.7x500 = 1350 km. On the other hand, by trading off temporal for spatial resolution as discussed in section 7.4, one could also retain 500-km spatial resolution by increasing the temporal resolution by a factor of $2.7^3 = 20$, from 3 min to about one hour.

9. Conclusions

The key factors which make radio sounding feasible in the magnetosphere are digital integration, tuned reception, and focusing by the magnetopause. Digital integration and tuned reception provide a combined gain of about 38 dB, equivalent to using a transmitter with 5000 times its actual radiated power. This increased equivalent power then makes it feasible to sound the plasmasphere with as little as 10 W and thanks to magnetopause focusing, to detect the magnetopause at a 30 kHz with an actual radiated power of only about 10 mW.

Equation (9) has been derived for the echo power flux of curved targets, and this formula has been evaluated for the magnetopause, plasmapause, and plasmasphere using a new analysis which allows for the varying radius of curvature of the plasmapause. Receiver tuning has been analyzed and it has been shown that this improves the signal-to-noise ratio by a factor of Q/2, where Q is the Q of the tuning inductor. A new method has been introduced for treating the receiver noise as an equivalent external noise flux. It has been shown how to measure echo directions from three-axis electric field measurements. It has also been shown that the angular resolution is twice the reciprocal signal-to-noise ratio, and finally, it has also been shown that the three-dimensional volume resolution is constant as the pulse length is varied.

It has been explained how AKR and escaping continuum can be eliminated by dynamic frequency selection, leaving trapped continuum below 30-40 kHz and cosmic noise above 100 kHz as the principal external noise sources for a magnetospheric sounder. The signal-to-noise ratio after digital integration for a typical measurement is found to be about 30 to 300 at frequencies of 30 to 300 kHz, thereby permitting direction measurements with an angular precision of about 0.4 to 4°.

A practical sounder for the magnetosphere would require a 3-kV, 10-W transmitter, orthogonal 400-m to 500-m tip-to-tip spin-plane antennas for transmission and reception, and a 10-m to 20-m tip-to-tip spin-axis antenna which would be used for reception only. This sounder would be capable of density measurements with 10% density resolution and 500 to 1350 km spatial resolution at target distances of 2 to 4 R_E in about 3 min.

Appendix A: Density Irregularities

The purpose of this appendix is to estimate the echo flux for density irregularities at the plasmapause and magnetopause. These irregularities will be modeled by an irregular rippled surface as shown in Figure 20, where the scale size of these ripples is larger than the wavelength and these ripples are assumed to be elongated along the magnetic field, perpendicular to the echo direction. Each ripple then produces echoes near its minima and maxima which add incoherently, producing an echo power flux according to Equation (9) which equals

$$\Phi_e = \frac{P\, n_{echo}}{16\,\pi\, s^2\,|1 + s/R|} \approx \frac{P\, n_{echo}\,|R|}{16\,\pi\, s^3} \tag{47}$$

where **P** is the effective radiated power, $\mathbf{n_{echo}}$ is the number of individual echoes contributing to the total echo, **s** is the distance, and $|\mathbf{R}|$ is the absolute value of the radius of curvature, assumed to be much less than **s**.

The dashed curves in Figure 20 indicate the region where these echoes contribute to a given range interval **Δs**, and for **Δs** « **s**, the lateral distance 2**d** over which such echoes contribute is

$$2d = 2\sqrt{(s+\Delta s)^2 - s^2} \approx 2\sqrt{2\,s\,\Delta s} \tag{48}$$

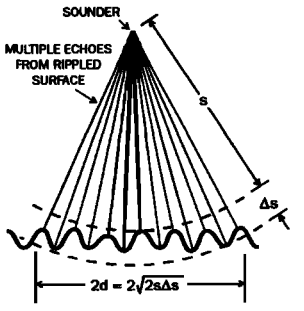

Figure 20. Multiple echoes from a rippled surface.

For a sinusoidal ripple of wavelength **b** and amplitude **a**, as shown in Figure 21, the radius of curvature at its minima and maxima is

$$R = \pm b^2/4\pi^2 a \tag{49}$$

and the number of echoes is

$$n_{echo} = 2\left[\frac{2d}{b}\right] = \frac{4\sqrt{2s\,\Delta s}}{b} \tag{50}$$

Substituting these into Equation (47) then gives

$$\Phi_e = \frac{P}{16\pi s^2}\left[\frac{\sqrt{2}}{\pi^2}\left(\frac{b}{a}\right)\sqrt{\frac{\Delta s}{s}}\right] \tag{51}$$

where the quantity in square brackets represents the echo flux relative to that of a plane reflector.

The strongest echoes should therefore come from weak, long-wavelength ripples for which **a** « **b**. For Δs = 500 km, the quantity $(\Delta s/s)^{1/2}$ varies from about 0.2 at **s** = 2 R_E to about 0.14 at **s** = 4 R_E. The quantity in square brackets for strong ripples with **a** ≈ **b** is therefore roughly 0.02 to 0.03, producing echoes which are weaker than specular reflection by about 15 to 17 dB.

On the other hand, for irregularities which are much smaller than the wavelength, the incoming wave should be scattered approximately uniformly over 2π radians in the plane perpendicular to the long dimension of the irregularity. In this plane the values of **x** and **y** which were used to derive Equation (6) would then become **x** = 2**d** from Equation (48) and **y** = π**s** for a complete semicircular arc, whereas in the plane of the irregularities one still has **y** = 2**x**. The echo flux for such omnidirectional scattering by thin field-aligned irregularities then becomes

$$\Phi_e = \frac{P}{4\pi s^2}\left(\frac{2d}{\pi s}\right)\left(\frac{1}{2}\right) = \frac{P}{16\pi s^2}\left[\frac{4\sqrt{2}}{\pi}\sqrt{\frac{\Delta s}{s}}\right] \tag{52}$$

In this case the quantity in square brackets becomes 0.25 to 0.36 and such echoes are therefore only 4 to 6 dB weaker than specular reflection by a smooth surface.

Equations (51) and (52) thus bracket the expected echo fluxes from an irregular rippled surface, suggesting that these spread echoes should be roughly 4 to 17 dB weaker than those for a smooth surface. For a magnetospheric sounder, on the other hand, in which the echo direction can be measured independently for each delay and doppler shift, it then becomes possible to measure density in three dimensions when such spread echoes occur, and the resulting angular resolution at 100 kHz according to Equation (36) should then be about 0.6° to 2.8°.

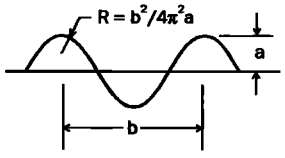

Figure 21. Amplitude **a**, wavelength **b**, and radius **R** of a sinusoidal ripple.

Appendix B: Plasmapause Curvature

This appendix includes a derivation of Equations (12) and (13) for the radii of curvature of the plasmapause, where R_1 is the radius of curvature in the magnetic meridian and R_2 is the azimuthal radius of curvature in the plane perpendicular to the magnetic meridian. These are the two principal radii of curvature of this surface.

The plasmapause is assumed to be symmetrical and given by Equation (10). Figure 22 shows a small arc **AB** of this surface in the magnetic meridian, of length **x** and having its center of curvature at point **C**. In this figure, λ_m is the magnetic latitude of point **A** and $\lambda_m + d\lambda_m$ is the magnetic latitude of point **B**.

The dip angle **I** in Equation (11) equals the angle between the radius vector and surface normal, as shown in Figure 22, where **I** is the dip angle at point **A** and **I** + **dI** is the dip angle at point **B**. The angle which is subtended by **x** at its center of curvature is thus $d\lambda_m$ + **dI**, and therefore

$$x = R_1\,(d\lambda_m + dI) \tag{53}$$

where for the triangle **ABD**

$$x = \sqrt{r^2 d\lambda_m^2 + dr^2} \tag{54}$$

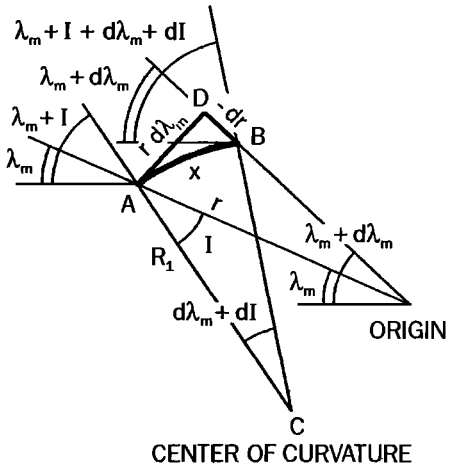

Figure 22. A segment **x** = **AB** of the plasmapause in the magnetic meridian, having a center of curvature **C** and subtending a magnetic latitude interval $d\lambda_m$.

where **r** is the radial distance of point **A** and **r** + **dr** (where **dr** is negative) is the radial distance of point **B**. Solving these two equations for $\mathbf{R}_1$ then yields

$$R_1 = \frac{\sqrt{r^2 + (dr/d\lambda_m)^2}}{1 + dI/d\lambda_m} \quad (55)$$

Differentiating Equations (10) and (11) and substituting from Equation (11) to eliminate λ_m then gives

$$dr/d\lambda_m = -2L\cos\lambda_m \sin\lambda_m = -r\tan I \quad (56)$$

and

$$dI/d\lambda_m = 2\sec^2\lambda_m \cos^2 I = \frac{1+3\cos^2 I}{2} \quad (57)$$

whereupon substituting these into Equation (55) then gives

$$R_1 = \frac{2r}{(3\cos^2 I + 1)\cos I} \quad (12)$$

As shown in Figure 23, the azimuthal center of curvature **C** for a point **A** on a figure of revolution always lies along its axis of symmetry. Where **I** is the dip angle at point **A**, λ_m is its magnetic latitude, and $\mathbf{R}_2$ is the azimuthal radius of curvature, the law of sines for the triangle **ABC** in Figure 23 then gives

$$\frac{R_2}{\cos\lambda_m} = \frac{r}{\cos(\lambda_m + I)} \quad (60)$$

whereupon solving for $\mathbf{R}_2$ and using Equation (11) to eliminate λ_m gives

$$R_2 = \frac{2r\cos I}{3\cos^2 I - 1} \quad (13)$$

As discussed above, this radius of curvature becomes infinite where cos **I** = $1/\sqrt{3}$, and hence where **I** = 54.7^0, λ_m = 35.3, and the dip angle equals the colatitude. This corresponds to the horizontal tangent at point **D** in Figure 23 where the plasmapause becomes flat in the azimuthal direction.

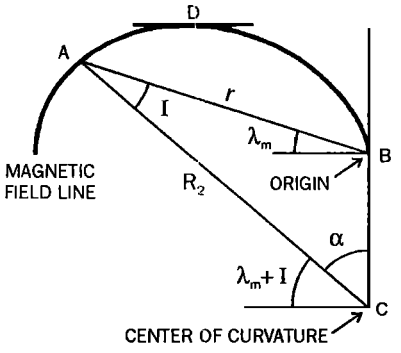

Figure 23. Plasmapause segment **AB** for which the azimuthal radius of curvature $\mathbf{R}_2$ is the distance to its center of curvature **C** on the axis of symmetry.

Acknowledgments. This paper is based on the pioneering work of Colin Franklin and John Jackson during the Alouette and ISIS Topside Sounder Programs and is dedicated to the memory of David Florida and John Chapman of DRTE (now CRC) in Canada. The authors also acknowledge useful suggestions by the Inner Magnetosphere Imager (IMI) Study Team headed by Tom Armstrong. This work was supported at the University of Iowa by NASA grants NAG5-1926 and NAG8-1030, at the University of Massachusetts Lowell by NASA grant NAG5-1055, and at Nichols Research Corporation by NASA contracts S07854-F and S22835-2.

References

Allis, W. P., S. J. Buchsbaum, and A. Bers, *Waves in Anisotropic Plasmas*, MIT Press, Cambridge, Mass., 1963.

Appleton, E. V., Wireless studies of the ionosphere, *J. Inst. Elect. Eng., 71*, 642-650, 1932.

Balmain, K. G., The impedance of a short dipole in a magnetoplasma, *IEEE Trans. Antennas Propag., 12*, 605-617, 1964.

Baumback, M. M., and W. Calvert, The minimum bandwidths of auroral kilometric radiation, *Geophys. Res. Lett., 14*, 119-122, 1987.

Bennett, W. R., *Electrical Noise*, McGraw-Hill, New York, 1960.

Benson, R. F., W. Calvert, and D. M. Klumpar, Simultaneous wave and particle observations in the auroral kilometric radiation source region, *Geophys. Res. Lett., 7*, 959-962, 1981.

Benson, R. F., M. M. Mellott, R. L. Huff, and D. A. Gurnett, Ordinary mode auroral kilometric radiation fine structure observed by DE 1, *J. Geophys. Res., 93*, 7515-7520, 1988.

Bougeret, J. L., J. Fainberg, and R. G. Stone, Interplanetary radio storms, *Astron. Astrophys., 136*, 255-262, 1984.

Breit, G., and M. A. Tuve, A test for the existence of the conducting layer, *Phys. Rev., 28*, 554-575, 1928.

Budden, K. G., *The Propagation of Radio Waves*, Cambridge Univ. Press, New York, 1985.

Calvert, W., Oblique Z-mode echoes in the topside ionosphere, *J. Geophys. Res., 71*, 5579-5583, 1966.

Calvert, W., The auroral plasma cavity, *Geophys. Res. Lett., 8*, 919-921, 1981a.

Calvert, W., The detectability of ducted echoes in the magnetosphere, *J. Geophys. Res., 86*, 1609-1612, 1981b.

Calvert, W., and G. B. Goe, Plasma resonances in the upper atmosphere, *J. Geophys. Res., 68*, 6113-6120, 1963.

Calvert, W., J. R. McAfee, R. B. Norton, T. L. Thompson, J. M. Warnock, and E. C. Whipple, A plasmapause sounder satellite, *NOAA Tech. Rep. ERL 242-AL-8*, 1972.

Carpenter, D. L., The Earth's plasmasphere awaits rediscovery, *EOS Trans. AGU, 76*, 89-92, 1995.

Carpenter, D. L., and R. R. Anderson, An ISEE/whistler model of equatorial electron density in the magnetosphere, *J. Geophys. Res., 97*, 1097, 1992.

Carpenter, D. L., B. L. Giles, C. R. Chappell, P. M. E. Décréau, A. M. Persoon, A. J. Smith, Y. Corcuff, and P.

Canu, Plasmasphere dynamics in the duskside bulge region: A new look at an old topic, *J. Geophys. Res., 98,* 19,243-19,271, 1993.

Chan, K. L., and L. Colin, Global electron density distributions from topside soundings, *Proc. IEEE, 57,* 1609-1612, 1969.

Chappell, C. R., Detached plasma regions in the magnetosphere, *J. Geophys. Res., 79,* 1861, 1974.

Davies, K., *Ionospheric Radio,* Peter Peregrinus Ltd., Short Run Press, Exeter, 1990.

Dyson, P. L., and R. F. Benson, Topside sounder observations of equatorial bubbles, *Geophys. Res. Lett., 5,* 795-798, 1978.

Etcheto, J., and J. J. Bloch, Plasma density measurements from the GEOS-2 relaxation sounder, *Space Sci. Rev., 22,* 597-610, 1978.

Franklin, C. A., and M. A. Maclean, The design of swept-frequency topside sounders, *Proc. IEEE, 57,* 897-929, 1969.

Green, J. L., and S. F. Fung, Radio sounding of the magnetosphere from a lunar-based VLF array, *Adv. Space Res., 14,* 217 1994.

Gurnett, D. A., and R. R. Anderson, The kilometric radio emission spectrum: Relationship to auroral acceleration processes, in *Physics of Auroral Arc Formation, Geophys. Monogr. Ser.,* vol. 25, edited by S-I. Akasofu and J. R. Kan, pp. 341-350, AGU, Washington, D.C., 1981.

Gurnett, D. A., W. Calvert, R. L. Huff, D. Jones, and M. Sugiura, The polarization of escaping continuum radiation, *J. Geophys. Res., 93,* 12,817-12,825, 1988.

Hagg, E. L., Electron densities of 8-100 cm^{-3} deduced from Alouette II high latitude ionograms, *Can. J. Phys., 45,* 27, 1967.

Haines, D. M., A portable digital ionosonde using coherent spread-spectrum waveforms for remote sensing of the ionosphere, Ph. D. thesis, Univ. of Mass. Lowell, Lowell, Mass., 1994.

Hartz, T. R., Radio noise levels within and above the ionosphere, *Proc. IEEE, 57,* 1042-1050, 1969.

Hashimoto, K., and W. Calvert, Observation of the Z mode with DE 1 and its analysis by three-dimensional ray tracing, *J. Geophys. Res., 95,* 3933-3942, 1990.

Huang, X., and B. W. Reinisch, Automatic calculation of electron density profiles from digital ionograms, *Radio Sci., 17,* 837-844, 1982.

Jackson, J. E., Reduction of topside ionograms to electron-density profiles, *Proc. IEEE, 57,* 960-975, 1969a.

Jackson, J. E., Comparison between topside and ground-based soundings, *Proc. IEEE, 57,* 976-985, 1969b.

Jackson, J. E., Alouette-ISIS program summary, *Rep. 86-09,* Natl. Space Sci. Data Cent., Greenbelt, Md, 1986.

Jackson, J. E., Results from Alouette 1, Explorer 20, Alouette 2 and Explorer 31, *Rep. 88-10,* Natl. Space Sci. Data Cent., Greenbelt, Md, 1988.

Jackson, J. E., E. R. Schmerling, and J. H. Whitteker, Mini-review on topside sounding, *IEEE Trans. Antennas Propag., 28,* 284-288, 1980.

James, H. G., Guided Z mode propagation observed in the OEDIPUS A tethered rocket experiment, *J. Geophys. Res., 96,* 17,865-17,878, 1991.

Jordan, E. C., *Electromagnetic Waves and Radiating Systems,* Prentice-Hall, Englewood Cliffs, N. J., 1950.

Knecht, R. W., T. E. VanZandt, and S. Russell, First pulsed radio soundings of the topside of the ionosphere, *J. Geophys. Res., 66,* 3078-3081, 1961.

Kurth, W. S., D. A. Gurnett, and R. R. Anderson, Escaping nonthermal continuum radiation, *J. Geophys. Res., 86,* 5519-5531, 1981.

Kurth, W. S., Detailed observations of the source of terrestrial narrowband electromagnetic radiation, *Geophys. Res. Lett, 9,* 1341-1344, 1982.

Lockwood, G. E. K., and G. L. Nelms, Topside sounder observations equatorial anomaly in the 75°W longitude zone, *J. Atmos. Terr. Phys, 26,* 569-580, 1964.

Muldrew, D. B., Radio propagation along magnetic field-aligned sheets of ionization observed by the Alouette topside sounder, *J. Geophys. Res., 68,* 5355-5370, 1963.

Nelms, G. L., and G. E. K. Lockwood, Early results from the topside sounder in the Alouette II satellite, in *Space Research III,* edited by R. L. Smith-Rose, pp. 604-623, North-Holland, New York, 1967.

Petrie, L. E., E. L. Hagg, and E. S. Warren, The influence of focusing on the apparent reflection coefficient of the F Region, *J. Geophys. Res., 70,* 4347-4356, 1965.

Ratcliffe, J. A., *The Magnetoionic Theory and its Application to the Ionosphere,* Cambridge Univ. Press, New York, 1959.

Reiff, P. H., J. L. Green, R. F. Benson, D. L Carpenter, W. Calvert, S. F. Fung, D. L. Gallagher, B. W. Reinisch, M. F. Smith, and W. W. L. Taylor, Radio imaging of the magnetosphere, *EOS Trans. AGU, 75,* 129-134, 1994.

Reinisch, B. W., New techniques in ground-based ionospheric sounding and studies, *Radio Sci., 21,* 331-341, 1986.

Reinisch, B. W., D. M. Haines, and W. S. Kuklinski, The new portable Digisonde for vertical and oblique sounding, *AGARD Conf. Proc.,* AGARD-CP-502, Feb. 1992.

Schmerling, E. R., and R. C. Langille, Introduction (to special issue on topside sounding), *Proc. IEEE, 57,* 859-860, 1969.

Stix, T. H., *The Theory of Plasma Waves,* McGraw-Hill, New York, 1962.

R. F. Benson, S. F. Fung, J. L. Green, and M. F. Smith, NASA Goddard Space Flight Center, Greenbelt, MD 20771.

W. Calvert, Department of Physics and Astronomy, University of Iowa, Iowa City, IA 52242.

D. L. Carpenter, StarLab, Stanford University, Stanford, CA 94305.

D. L. Gallagher, Marshall Space Flight Center, Huntsville, AL 35812.

D. M. Haines and B. W. Reinisch, University of Massachusetts Lowell, Lowell, MA 01854.

P. H. Reiff, Rice University, Houston, TX 77251.

W. W. L. Taylor, Nichols Research Corporation, Arlington, VA 22209.

(Received October 28, 1994; revised May 23, 1995; accepted June 7, 1995)